Journal of
Marine Science and Engineering

MDPI

Article

Observation and Modeling of Nonlinear Internal Waves on the Sea of Japan Shelf

Igor Yaroshchuk [1,*], Valery Liapidevskii [2], Alexandra Kosheleva [1], Grigory Dolgikh [1], Alexander Pivovarov [1], Aleksandr Samchenko [1], Alex Shvyrev [1], Oleg Gulin [1], Roman Korotchenko [1] and Fedor Khrapchenkov [1]

[1] V.I. Il'ichev Pacific Oceanological Institute, Far Eastern Branch, Russian Academy of Sciences, 690041 Vladivostok, Russia; samchenco.an@poi.dvo.ru (A.S.)
[2] Lavrentyev Institute of Hydrodynamics, Siberian Branch, Russian Academy of Sciences, 630090 Novosibirsk, Russia; vliapid@mail.ru
* Correspondence: yaroshchuk@poi.dvo.ru

Abstract: This paper presents a discussion on observations of nonlinear internal waves (NLIWs) in the coastal zone of the Sea of Japan, based on the mooring of thermostring clusters in different seasons of 2022. For statistical evaluation of the frequency of event occurrence and determination of NLIW movement direction, we use our observations of the past 12 years. We present the NLIW structures, observed in spring, summer, and autumn of 2022, which are typical for this shelf area. Two types of nonlinear waves are described—solitary and undular bores, with or without strong vertical mixing behind the front. We demonstrate spatial transformation of an undular bore as it moves over the shelf. A mathematical model based on the second-order shallow water approximation is proposed for numerical simulation. To simplify calculations, the authors limit themselves to two- and three-layer shallow water models. We investigate the possibility of spatiotemporal reconstruction of internal nonlinear structures between thermostrings using experimental data and proposed models. The authors show that at distances of up to several kilometers between thermostrings, the wave fields of strongly nonlinear and nonstationary structures can be successfully reconstructed. Water flow induced by NLIWs can be reconstructed from the data of even one thermostring.

Keywords: nonlinear internal waves; numerical simulation; Green–Naghdi equations; thermistor string; shelf; the Sea of Japan

Citation: Yaroshchuk, I.; Liapidevskii, V.; Kosheleva, A.; Dolgikh, G.; Pivovarov, A.; Samchenko, A.; Shvyrev, A.; Gulin, O.; Korotchenko, R.; Khrapchenkov, F. Observation and Modeling of Nonlinear Internal Waves on the Sea of Japan Shelf. *J. Mar. Sci. Eng.* **2024**, *12*, 1301. https://doi.org/10.3390/jmse12081301

Academic Editor: Angelo Rubino

Received: 3 July 2024
Revised: 25 July 2024
Accepted: 30 July 2024
Published: 1 August 2024

1. Introduction

Internal waves (IWs) in the ocean are perturbations of the water density distribution over depth that propagate over large horizontal distances in a vertically inhomogeneous fluid with thermohaline stratification.

In the shelf zone of the ocean, in addition to the internal waves that originate in the open sea and travel toward the coast, there are always IWs generated by dynamic processes over the continental slope. These waves are nonlinear internal waves (NLIWs) and manifest themselves as long waves with tidal and inertial periods, and as soliton-like wave packets [1,2]. Regular transfer of tidal energy from the areas of the continental slope to the coast is provided by internal tidal waves. As they pass over the shelf and interact with the shelf edge and bottom topography, the internal tides undergo a nonlinear transformation. As a result of this transformation, they produce packets of intense short waves that, like the long wave that generated them, continue to move toward the coast until they reach the coastal zone, where wave energy is further transferred to the shorter wavelength range and into turbulence [3].

Submesoscale vortices and wind fluctuations of currents in the continental slope zone can play a noticeable role on the shelf. Inertial oscillations in the presence of currents and vortices in the continental slope zone generate inertial IWs, and their energy can transfer at the resonant (local inertial) frequency into inertial-gravity IWs. As a result, the maxima at semidiurnal and local inertial periods can alternate or appear simultaneously in the spectra of measured IWs [4].

To date, a large number of scientific publications have been devoted to field studies of IWs in various seas of the world's oceans. Theoretically studied in most detail are soliton-type NLIWs on the shelf, which can be modeled on the basis of nonlinear evolutionary equations with dispersion of the Korteweg–de Vries (KdV) and Gardner types [5–7], and also on the basis of Green–Naghdi-type equation systems [8,9].

One of the aims of such studies is to establish the relationship between the density stratification properties of an inhomogeneous fluid and the kinematic properties of nonlinear internal waves. A number of publications emphasize the solution of inverse problems. The interest in inverse problems is stimulated both by the concerns of modern oceanology and hydroacoustics, and by the modern possibilities of combining NLIW remote sensing methods with their direct thermohaline measurements. For example, some authors propose methods to reconstruct the density profile from known amplitude dispersion curves for solitary internal waves [10,11]. In [6,8], the authors proposed using field data obtained at buoy stations and subsequent numerical NLIW modeling to reconstruct the density (temperature) field in a coastal water area covered by a cluster of thermistor strings [12].

The experimental studies of NLIWs presented in this paper were carried out by the authors in the southwestern part of the Sea of Japan in Peter the Great Bay as a part of various projects to investigate hydroacoustic and seismoacoustic signals in the shelf zone of the Sea of Japan. In this paper, we discuss the 2022 experiments; however, we use the results of our research of the last 12 years (2012–2023) in analyzing the results, and in some sections of the paper. We should note that other authors have also investigated NLIWs in Peter the Great Bay in different years and by various methods. Most of the measurements were made by means of towed distributed temperature sensors on spatial sections, vertical measurements at stations across the shelf, registration of temperature and current variations at moored buoy stations near the shelf edge, and acoustic Doppler current profilographs onboard a moving vessel [13–16]. The authors of these works studied the spectral characteristics of IWs, and determined kinematic and nonlinear parameters and the movement directions of NLIW trains. Sinusoidal and soliton-like oscillations of the thermocline were described in [17,18].

Analysis of the results of numerous observations allowed it to be determined that on the shelf of Peter the Great Bay, NLIWs generated by barotropic tides above the continental slope in the 15–20 km area in front of the shelf edge are predominant [19]. In the autumn period, under the action of the northern monsoon, a water structure with significant temperature gradients is formed in this region. Therefore, intense internal wave activity is observed in autumn. In [20], the internal tide in the autumn period was studied and it was shown that temperature perturbations excited at the shelf edge propagate to the coastal zone approximately normal to isobaths, with a velocity close to a velocity of the first mode of IWs with the frequency of the tidal harmonic M_2. Estimates and calculations gave an approximate value of this velocity of 0.4 m/s. Video monitoring and field experiments revealed that in all seasons of the year, the phase speeds of NLIWs vary from 0.3 m/s to 0.5 m/s depending on hydrological conditions [21,22]. In [23], internal undular bores in this shelf region were studied, and it was found that they are of three types. Each type is determined by the position of a soliton with maximum amplitude in the train of internal soliton-like waves following the front. In a recent paper [24], the authors propose an atlas consisting of a set of maps of kinematic and nonlinear parameters of internal waves in the Sea of Japan, which allows zoning the water area by possible wave types and determining the polarities and maximum amplitudes of generated solitary waves. We also note that reference data on hydrology for different seasons of the year, based on our systematic studies over 12 years, are provided in Section 3, Observations of NLIWs.

The peculiarity of the experimental studies presented in this paper is that the authors used the long-term setups of two moored thermistor strings (thermostrings) clusters to record the NLIWs, normally to the isobaths, and approximately along the isobaths. Systematic mooring of thermostrings in different seasons of the year allowed the authors to collect valuable material that gave them an opportunity to analyze in detail the characteristics of the nonlinear transformation of the NLIWs as they moved toward the coast.

The purpose of the presented study is as follows:

- To investigate and evaluate general characteristics of NLIWs in the coastal zone of the Sea of Japan based on systematic mooring of thermistor string clusters in different seasons of the year.
- To develop and verify simple but effective NLIW modeling schemes.
- To investigate the possibility of space and time reconstruction of nonlinear structures between thermostrings. To efficiently reconstruct the wave field along selected directions.

The paper is organized as follows. In Section 2, we present a geographical description of the experimental study area; the locations of thermostring clusters are indicated. We review the experimental data by season. In Section 3, we discuss transformation of NLIWs as they move over the shelf, present examples of internal wave bores and NLIW trains, and analyze their kinematic characteristics. In Section 4, we propose two- and three-layer current models based on the shallow water equations, compare the results of calculations and field measurement data, and propose a methodology for reconstructing the temperature between thermostrings from numerical simulation results. In Section 5, we discuss mathematical models of NLIWs and summarize the results of field studies and numerical simulations.

2. Materials and Methods

The experimental results discussed below were obtained at the POI FEB RAS hydrophysical test site located in the southwestern part of Peter the Great Bay of the Sea of Japan. The main measuring hydrophysical instruments for the experiments were thermostrings, current meters, and CTD profilers [25]. Figure 1 shows in detail the site location and presents the scheme of the measuring equipment setup during three seasons of 2022.

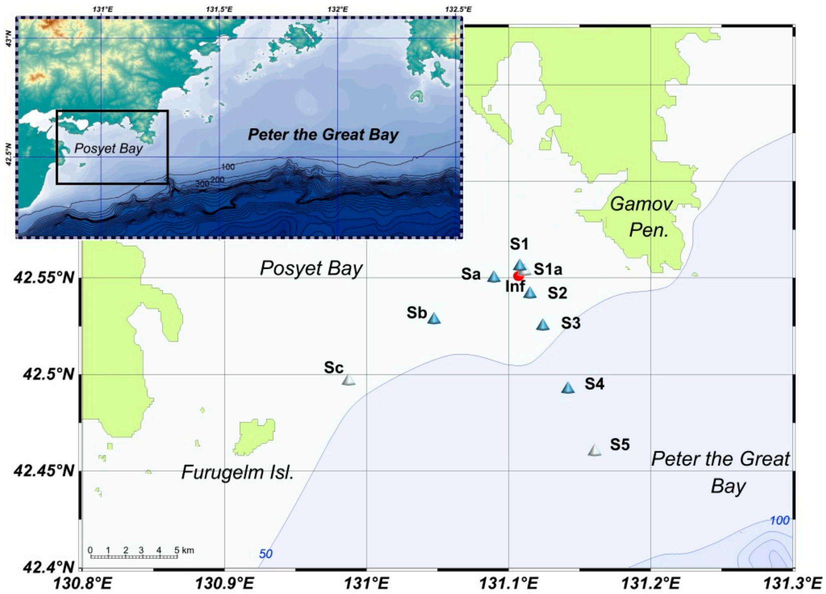

Figure 1. Scheme of thermostrings arrangement, triangles; the Infinity string is a red circle. Dark triangles indicate regular setups, light triangles indicate occasional moorings.

All thermostrings are labeled with the letter S and numbered for ease of subsequent discussion. They were arranged in two clusters: the first group of thermostrings was placed approximately normal to the isobaths from the side of the shelf break and had a direction of 336°; the second group, along the 40 m isobath. The sensors of almost all the thermostrings were arranged 1 m apart, and at the deep-water station S5 they were moored 3 m apart; they registered temperature every 1 s. However, we used temperature values averaged over 1 min for analysis and calculations [25]. In addition, we averaged temperature and currents over time intervals of 10, 20, and 60 min as needed.

CTD measurements were performed along two clusters of thermostrings taking into account the occurrence of various hydrometeorological events in the test site area [26]. Currents were recorded with Infinity electromagnetic current meters at three depths near the S1 shallow-water point at 1 min intervals.

The insert in Figure 1 shows the geographical location of the hydrophysical test site as a rectangle. A part of the site is located in the waters of Posyet Bay, one of the seven smaller bays within Peter the Great Bay, and a part is located directly in Peter the Great Bay—the largest bay of the Sea of Japan.

This area of the sea is characterized by a rather narrow shelf, 10–25 km wide. The shelf topography in this study area is characterized by a relatively smooth change in depth: up to 100 m isobaths, 5 m/km; from 100 m to 200 m isobaths, 20 m/km; and a further sharp shelf break 210 m/km in the depth range of 200 m to 2 km [26].

Figure 2 shows the arrangement of the first cluster of thermostrings in lateral projection, with depths and bottom topography, and the insert in the figure shows the bottom profile up to the shelf break.

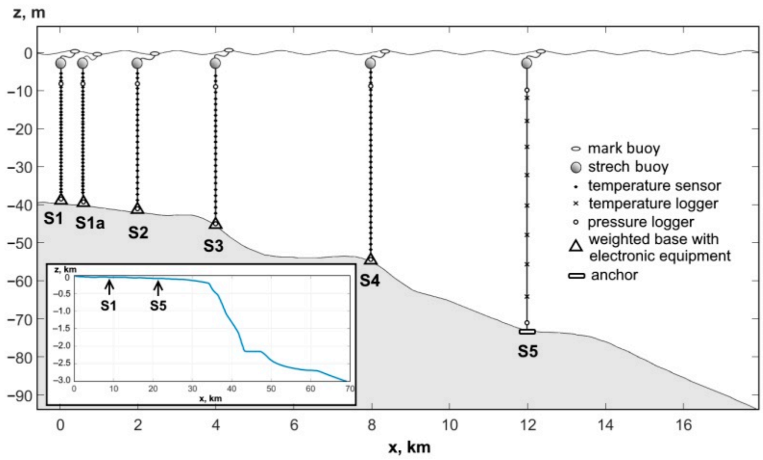

Figure 2. Scheme of thermostrings' arrangement and bottom relief topography in lateral projection. The inset shows the profile of the bottom up to the shelf break.

For numerical modeling of the NLIW reconstruction, we limited ourselves to the two- and three-layer shallow water equations proposed in [8]. In subsequent works by the authors [27,28], these equations and algorithms were modified and tested both on field marine data and on laboratory modeling data.

3. Observations of NLIWs

In this section, we discuss the peculiarities of the NLIW transformation based on temperature observations at different clusters of thermostrings. Let us first consider in general terms the variability in water temperature averaged over a time interval of 1 h. For an example, we choose one buoy: shallow-water station S1.

Figure 3 shows temperature distributions recorded by the S1 thermostring in different seasons of 2022: 24 May–7 June (331 h), 31 July–14 August (336 h), 3–14 October (257 h). The time in the graphs here and further in the text are given in hours from the beginning of the experiment.

The temperature distribution shown in Figure 3 demonstrates the typical dynamics of temperature stratification for this region. Thus, the variability in spring stratification is determined not only by radiative heating of the upper layer, but also by the advection of relatively warm water from the open part of the Sea of Japan to the shelf zone of the bay under the influence of the southern monsoon. The temperature distribution along the depth is predominantly linear, 0.1 °C/m, with thin layers with gradients up to 1 °C/m, with no stable upper homogeneous layer.

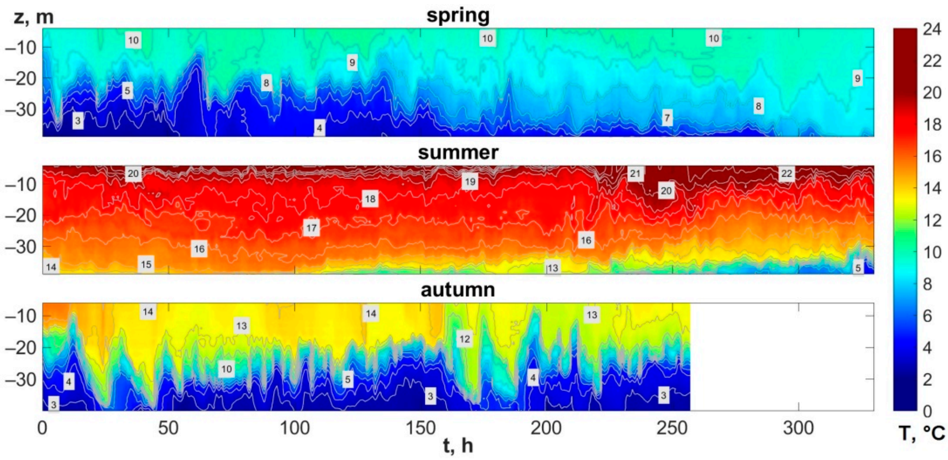

Figure 3. Temperature distribution on thermostring S1 in spring, summer, and autumn, averaged over a time interval of 1 h. The numbers indicate temperature values of isotherms shown in gray.

Summer thermal stratification is formed when the period of intensive radiation heating is over and the surface layer temperature increases to 24–26 °C. At the same time, low temperature values up to 1 °C are preserved in the bottom layer due to the inflow of cold water from the open part of the Sea of Japan, including tidal processes and the cold Primorsky Current. Due to intensive heating, temperature gradients of up to 3 °C/m and more are formed in the upper layer, at horizons to 6–10 m, while below there is a weak gradient layer of up to 0.2 °C/m enveloping the main water column. The near-bottom high-gradient layer of 1–4 °C/m is formed under the influence of dynamic processes observed in the bay [26].

In the autumn period, either a three- or two-layer water structure is formed due to sea cooling and under the action of the northern monsoon. Thus, during 5 out of 12 years of observations (2012–2023), a two-layer water structure was observed in autumn, when the upper layer was thermally quasi-homogeneous with a thickness of 25–35 m, and the lower layer of the thermocline was 5–15 m thick, with a gradient of 1–3 °C/m. During the other 7 out of 12 years, we observed a three-layer water structure. In this case, it was defined by pronounced homogeneous layers of 5–15 m in the upper and lower part of the layer and an intermediate layer of thermocline with a gradient up to 2.5 °C/m. We should note that in some cases a two-layer structure was transformed into a three-layer structure over time. This rearrangement of the water structure occurred due to the cold water inflow from the ocean during recurrent autumn upwelling [26].

Within the framework of the IWs' general description, let us now consider the frequency variability of the temperature field in the process of field observations. Experimental data, as a rule, are nonstationary, so we can use wavelet transform or Hilbert transform techniques to study the frequency spectrum in detail [29]. However, in this case, we will limit ourselves to the Fourier transform, which provides quality analysis of thermocline oscillations [30].

Figure 4 shows the frequency spectra of the isotherms' vertical oscillations inside the thermocline in different seasons of 2022. We know that oscillations in the thermocline in the ocean in the frequency range from the inertial frequency to the buoyancy frequency are mainly determined by the IWs. Therefore, for frequency analysis we selected isotherms that were predominantly inside the thermocline during the experiment. Isotherm T = 6 °C was selected for spring, T = 16 °C for summer, and T = 10 °C for autumn. For spectral analysis, we used series with 10-day durations, chose the sample length to be 4 days with an overlap of 50%, and used a Hamming window, with sampling frequency 1/60 Hz. We filtered out oscillations with periods of less than 5 min, and selected the frequency range in the graphs from 0.3 to 70 cycles per day (cpd). The inertial frequency for this area, at the latitude of 42.5 °N, is 0.056 cph (period = 17.7 h, gray arrows in Figure 4), the frequency of the semidiurnal tide is 0.08 cph (period = 12.4 h, black arrows in Figure 4). These frequencies were quite satisfactorily traced in the spring and autumn seasons of the year in the form of maxima on the graphs (see Figure 4a), but they were very inexpressive in the spectrum in summer. Perhaps this state of affairs is due in this case to the high activity of various dynamic processes in summer [26]. Using the same isotherms obtained from deeper water thermostrings does not significantly change the behavior of the spectra; see Figure 4b. In both figures, for illustration, the power function $f^{-3/2}$ is shown, which at high frequencies better describes the behavior of the spectrum than the f^{-2} function corresponding to the Garrett–Munk spectrum. Let us note that this behavior of the frequency spectrum in shelf zones is noted by various authors, for example, [31,32].

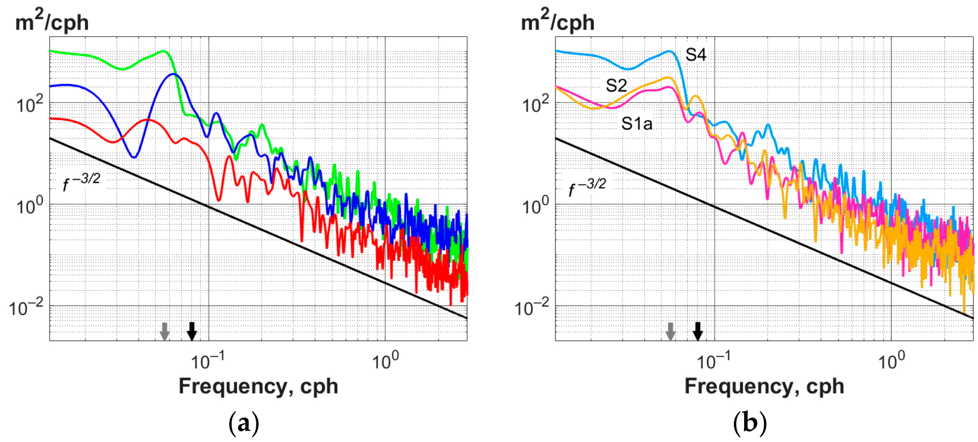

Figure 4. Frequency spectra of IW isotherms' vertical displacement in 2022: (**a**) spectra according to the S4 thermostring's data in spring—green line, in summer—red line, and in autumn—blue line; (**b**) spectra in spring at different stations S1a—pink line, S2—orange line, S4—blue line. Gray arrow indicates inertial frequency, black arrow indicates semidiurnal tidal frequency.

An important stage of the experimental research was to determine the direction of nonlinear IW motion. This information allowed us to further select simple and efficient mathematical models, which are discussed further in Section 4.

To ensure certainty in our selection of events, and following the recommendations of the authors in [18], we analyzed only intense internal waves, in which the range of vertical oscillations exceeded 5 m. As a rule, NLIW trains and internal bores with "tails" of soliton-like wave trains fell into this category.

Figure 5a shows the motion vectors of IWs in different seasons, determined using a triangle formed by S1 and two additionally installed systems; the sides of such triangles ranged from 100 m to 2 km in different years. For demonstration purposes, three years were selected for each season from the observation range of 2012–2023: spring of 2012, 2015, and 2016; summer of 2014, 2017, and 2019; and autumn of 2013, 2019, and 2021. The vector length corresponds to the speed of movement; it ranged from 0.1 to 0.6 m/s. The direction of movement of the wave front is indicated in degrees, where 0° corresponds to the direction to the north. As calculations showed, the main part of the IWs at the test site moved in the direction of 320–350°, i.e., with scatter of ±15° in the direction normal to the isobaths. Our cluster S5–S1 had approximately the same direction, 336°. However, in a number of cases in the autumn period we also recorded IWs moving north (0° ± 10°); such a change in direction was apparently caused by hydrometeorological events (HEs) [26]. Figure 5b shows histograms of NLIW manifestations recorded at two points of the test site in 2012–2023. As we can see from the Figure, IWs were most often recorded in autumn, least often in summer. In summer, as a rule, either oscillations with amplitudes of less than 5 m were observed, or there were long periods of several days without intense IWs, containing only weak background oscillations. This state of affairs is explained by the intense heating of the water layer towards the end of summer, when its column eventually becomes quasi-homogeneous. However, after the onset of the next HE, influx of cold waters from the ocean occurs and stratification can become quite pronounced, which causes the appearance of intense IWs.

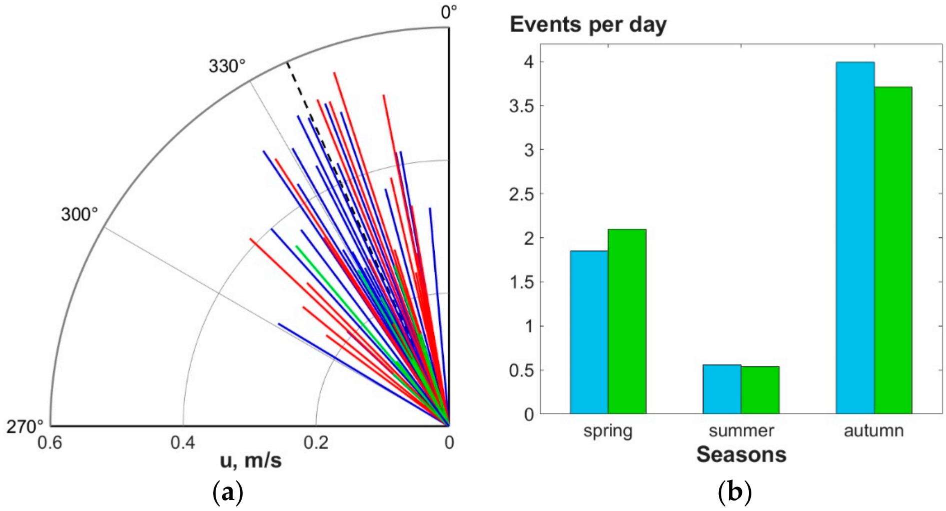

Figure 5. Direction and speed of intense IW movement (**a**): green lines—in spring, red—in summer, blue—in autumn; the dotted line shows the direction of the S5–S1 cluster at 336°. Histograms of registration of IW manifestations in spring, summer, and autumn (**b**): blue bars—recorded at station S1, green—at station S4.

Turning back to the analysis of NLIW manifestations, in addition to Figure 3, we now consider temperature distribution over depth in more detail. Figures 6–8 show isotherms at 1–2 °C at stations S4, S3, and S1 in different seasons of 2022. For clarity, observation time intervals were chosen to be a little over two days in order to show as many events as possible, such as wave depressions, packages of short-period NLIWs, and internal bores. All isotherms were plotted using temperature series averaged over the time interval of 1 min.

As we noted above, in spring, water masses are characterized by weak stratification. Figure 6 shows long-wave oscillations associated with tides, and also shows formation of short-period wave packets in areas where isotherms are concentrated, i.e., in thin layers with moderate temperature gradients.

Figure 7 shows isotherms at every 2 °C over two days. In summer, the waters are characterized by layers of water with large gradients. Formation of temperature depressions and NLIW packets was observed. Bottom lenses of cold water formed near the bottom [33]. The black rectangle at the top of Figure 7 marks the NLIW package which is used for numerical modeling in Section 4.

The autumn water structure is characterized by a fairly stable bottom thermocline. Such stratification under the influence of semidiurnal tides leads to the active formation of soliton-like waves and internal wave bores [20,34]. Such phenomena are well known and have been observed by many researchers in various coastal zones of the world's oceans [2]. Figure 8 shows well-defined long waves of depression in the deep-water part of the measuring complex (S3, S4), associated with the internal tide, and moving along the shelf toward the shore. When a wave enters the shallow area (S1a), the leading front of the wave flattens, and the trailing front steepens and transforms into an internal bore [35].

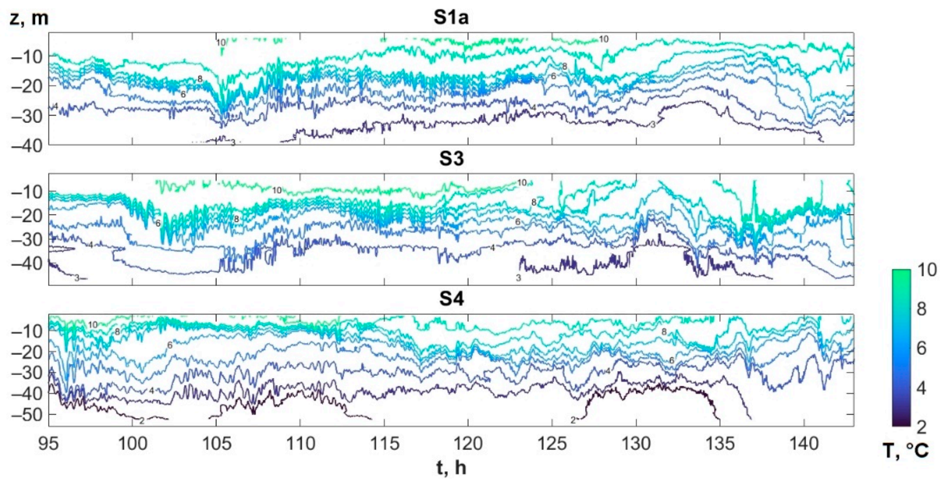

Figure 6. Isotherms for two days of the experiment at points S4, S3, and S1a in the spring of 2022 (averaging data over the time interval of 1 min). Isotherms at every 1 °C.

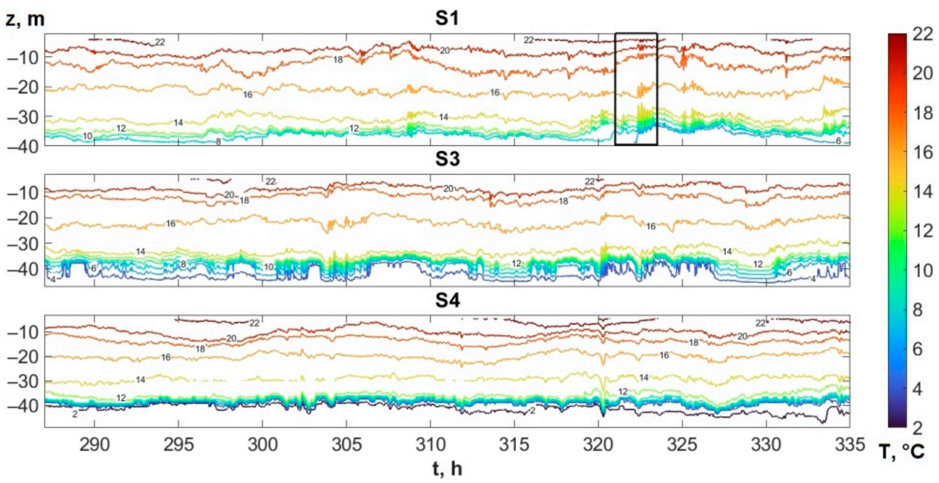

Figure 7. Isotherms for two days of the experiment at points S4, S3, and S1 in the summer of 2022 (averaging data over the time interval of 1 min). Isotherms at every 2 °C. The rectangle marks the NLIW package discussed in Section 4.

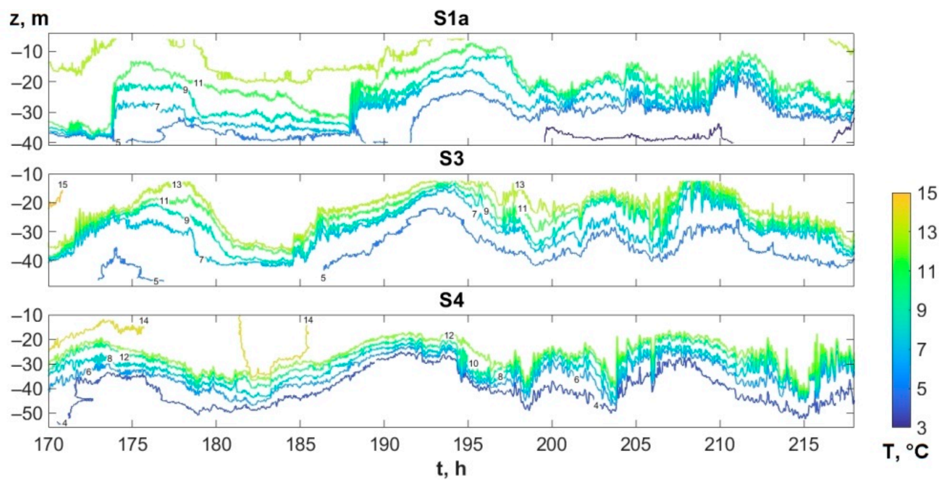

Figure 8. Isotherms for two days of the experiment at points S4, S3, and S1a in autumn of 2022 (averaging data over the time interval of 1 min). Isotherms at every 2 °C.

Moving toward the shore, the structure of the bore undergoes consistent changes. As an example, Figure 9 shows two stages of internal bore development. Figure 9a shows an internal bore, which some authors call a "bore alone" [36]. The bore alone and the stratification disturbances caused by it are observed in the time interval t = 174 h–178 h. In the case when the thermocline in front of the wave is "pressed" to the bottom, immediately after a sharp jump in temperature, the isotherms, performing chaotic movements, "scatter" in depth, abruptly changing the water stratification. This corresponds to the situation when a two-layer stratification in front of the disturbance front is transformed into stratification with continuous temperature distribution directly behind the front, and the wave motion takes on a multimode character. The second case, shown in Figure 9b, demonstrates transformation of a disturbance into an undular bore, where the thermocline largely retains its characteristics, but oscillates up and down. Here, we can clearly see the birth of a train of solitons at the leading front of the bore. Some authors call this structure a "solibore" [37,38]. This state of affairs corresponds to the case when the wave motion is determined mainly by the first mode [39].

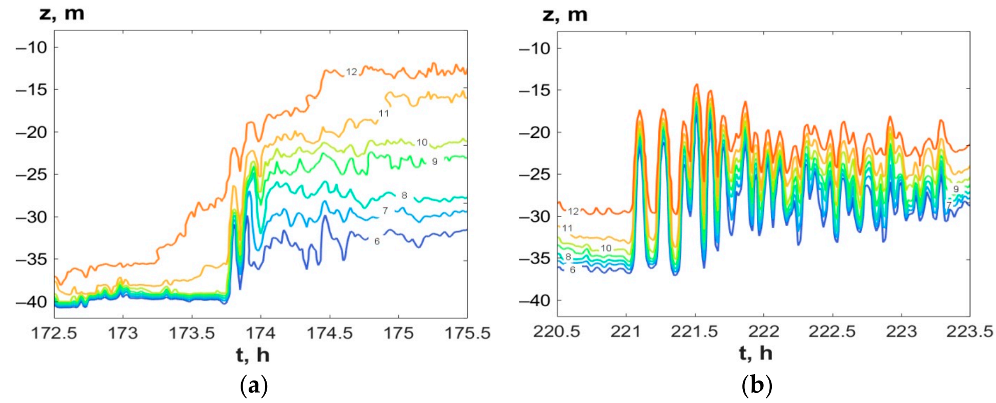

Figure 9. Bores in autumn 2022: (**a**) bore alone registered on S1a; (**b**) undular bore registered on S1a.

Figure 10 demonstrates the evolution of stratification during the passage of alone and undular bores, and some time after these events. As we can see in Figure 10a, before the arrival of a bore alone, the water stratification was determined by a fairly strong bottom thermocline with gradient $\partial T/\partial z$ = 1.3 °C/m (blue line). After the passage of the bore, in a little over an hour, the waveguide structure of the stratification collapsed and degenerated into being linear from the surface to the bottom with a weak gradient $\partial T/\partial z$ = 0.24 °C/m (green line). In 4–5 h from the beginning of the event, the original structure of the waveguide began to recover—the black line demonstrates formation of several thermoclines.

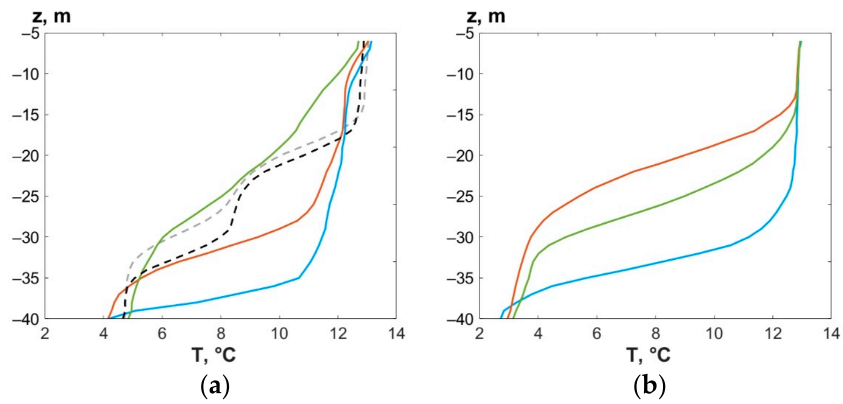

Figure 10. (**a**) Temperature variability during bore alone passage at point S1a: blue line t = 173.7 h, red line t = 173.8 h, green line t = 175 h, gray line t = 178 h, black line t = 178.2 h. (**b**) Temperature variability during passage of the undular bore: blue line t = 221 h, red line t = 221.5, green line t = 223.3 h.

Figure 10b shows the effect of undular bore stratification. Before the passage of the bore, the near-bottom thermocline was described by a gradient $\partial T/\partial z$ = 1.1 °C/m (blue line). During the passage of the solibore, the gradient was $\partial T/\partial z$ = 0.7 °C/m (red line), and the depth of the thermocline was approximately 40–25 m. After the passage of the soliton train, the gradient was $\partial T/\partial z$ = 0.8 °C/m (green line), and the depth of the thermocline changed slightly, becoming 30–15 m. Thus, in this case, the thermocline mainly retained its characteristics, but the gradient became somewhat weaker.

The last figure in this section, Figure 11, demonstrates the process of evolution of a wave bore in space and time. Here, the passage of an undular bore is shown by measurements of a cluster of thermostrings at points S4, S3, S2, and S1a.

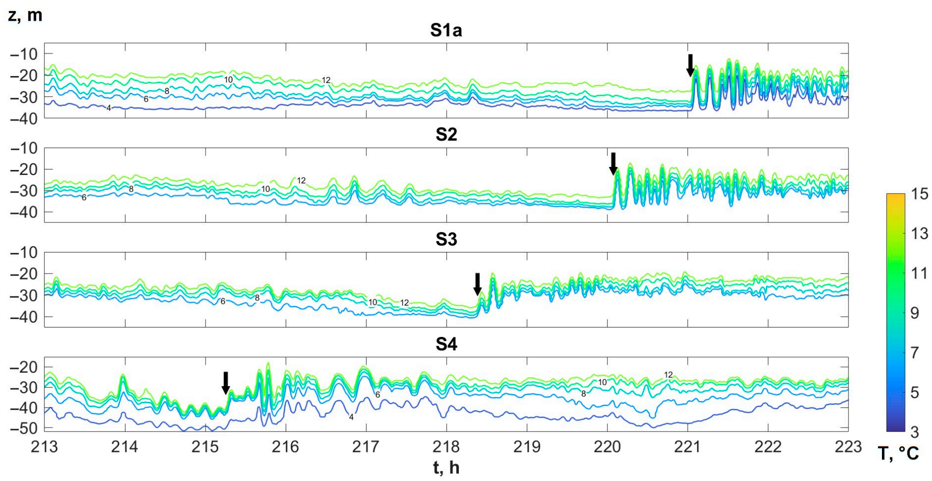

Figure 11. Space–time evolution of wave bore. Black arrows show the leading front of the solibore.

When moving along the S4–S1a path, the undular internal bore retains a specific configuration—a depression wave, followed by a density jump and a train of soliton-like waves. It allowed us to track the passage of this bore along a cluster of thermostrings and estimate the phase velocity of the solibore movement. This was 0.35 m/s when moving from station S4 to S3 and further to S2, and 0.37 m/s between stations S2 and S1. In Figure 11, we can see that when the solibore moves towards the shore, there is a slight increase in the amplitudes of soliton-like waves near its leading front.

4. Mathematical Models of NLIW

In this section, we limit ourselves to three- and two-layer shallow water models obtained in the second order of smallness in terms of the parameter $\varepsilon = H^2/L^2$, where H is the thickness of the fluid flow channel and L is the characteristic wavelength. Numerous calculations and subsequent comparisons of them with the results of field observations in different years have shown that these models are sufficient for solving the problems we set; see, for example, [8,33].

Next, we consider a class of stratified fluid flows under the assumption that the length of internal waves significantly exceeds the channel depth. In the model, we consider the influence of vertical acceleration of fluid particles on the position and shape of the wave front. In the framework of the three-layer flow model, we assume that the fluid consists of three homogeneous layers with density $\rho_1 < \rho_2 < \rho_3$ under the condition $(\rho_3 - \rho_1)/\rho_1 << 1$. We also assume that the pressure in the intermediate layer is distributed according to the hydrostatic law. This assumption is based on the fact that the thickness of this interlayer is small compared to the thickness of the outer layers, and it is also based on the peculiarities of short-wave generation and collapse processes in the interlayer after the passage of long waves [40].

4.1. Governing Equations

In the Boussinesq approximation [41], the equations of three-layer flow of weakly density-stratified fluid in the gravity field take the following form:

$$
\begin{aligned}
&h_{1t} + (h_1 u_1)_x = 0,\ h_{2t} + (h_2 u_2)_x = 0,\ h_{3t} + (h_3 u_3)_x = 0,\\
&u_{1t} + \left(\tfrac{1}{2}u_1^2 + p\right)_x + \tfrac{1}{3h_1}\left(h_1^2 \tfrac{d_1^2 h_1}{dt^2}\right)_x = f_1,\\
&u_{2t} + \left(\tfrac{1}{2}u_2^2 + b_2(h_3 + h_2 + z) + p\right)_x = f_2,\\
&u_{3t} + \left(\tfrac{1}{2}u_3^2 + b_3(h_3 + z) + b_2 h_2 + p\right)_x + \tfrac{1}{3h_3}\left(h_3^2 \tfrac{d_3^2 h_3}{dt^2}\right)_x = f_3,\\
&b_2 = (\rho_2 - \rho_1)g/\rho_1,\ b_3 = (\rho_3 - \rho_1)g/\rho_1,\\
&\tfrac{d_1}{dt} = \tfrac{\partial}{\partial t} + u_1 \tfrac{\partial}{\partial x},\ \tfrac{d_3}{dt} = \tfrac{\partial}{\partial t} + u_3 \tfrac{\partial}{\partial x},\\
&H = \sum_{j=1}^{3} h_j, \qquad Q(t) = \sum_{j=1}^{3} h_j u_j,\ H + z = \text{const}.
\end{aligned}
\tag{1}
$$

Here, ρ_j is the density of water and u_j is the velocity of water in the j-th layer, and h_j is the thickness of the j-th layer, (j = 1, 2, 3). The layers are numbered from top to bottom; the equation $z = z(x)$ defines the bottom topography; g is the acceleration of gravity; b_2 and b_3 are buoyancy coefficients; $p = p_1/\rho_1$, p_1 is the pressure at the upper boundary of the flow; t is time, and x is the horizontal coordinate. Let us note that in the Boussinesq approximation the upper boundary of the flow is horizontal, which allows us to exclude surface waves from consideration.

The functions f_j in Equation (1) specify friction at the layers' boundaries and at the bottom when dissipative effects (parameter c_1) are taken into account [42]. Dissipation of internal wave energy in a multi-layer medium is mainly determined by mixing and generation of short waves at the internal boundaries of the flow. Bottom friction also influences the evolution of near-bottom internal waves and can be included in the flow model (parameter c_2):

$$
\begin{aligned}
f_1 &= -\frac{c_1(u_1 - u_2)|u_1 - u_2|}{h_1},\\
f_2 &= -\frac{c_1(u_2 - u_3)|u_2 - u_3| + c_1(u_2 - u_1)|u_2 - u_1|}{h_2},\\
f_3 &= -\frac{c_2 u_3 |u_3| + c_1(u_3 - u_2)|u_3 - u_2|}{h_3}.
\end{aligned}
$$

The consequence of (1) for incompressible fluid is the dependence of the total water flow quantity through an arbitrary cross-section of the channel $Q(t)$ on time only. The value of $Q(t)$ is considered to be further known by virtue of the given boundary conditions. Therefore, after excluding the variables h_2, u_2, and p, System (1) is reduced to four equations for the function h_3, h_1, u_3, and u_1. Equation (1) allow us to describe the evolution of nonlinear internal waves of the first and second modes, and also their interaction. However, the system is still complicated enough for construction of partial solutions and numerical study of nonstationary wave processes. Let us note also that the hydrostatic condition in the interlayer does not affect the structure of bottom waves of large amplitude, since the main perturbation of the internal boundaries of the interface during passage of the waves is associated with deformation of the lower bottom layer, while the interlayer remains relatively thin.

To perform numerical analysis of nonstationary strongly nonlinear wave processes, it is reasonable to represent Equation (1) in the following divergent form [9]:

$$
\begin{aligned}
&h_{1t} + (h_1 u_1)_x = 0,\ h_{3t} + (h_3 u_3)_x = 0,\ R_t + \left(Ru_1 - \frac{1}{2}u_1^2 + p - \frac{1}{2}h_1^2 u_{1x}^2\right)_x = f_1, \\
&u_{2t} + \left(\frac{1}{2}u_2^2 + b_2(h_3 + h_2 + z) + p\right)_x = f_2,\ E_t + \left(Eu_3 - \frac{1}{2}u_3^2 + b_3(h_3 + z) + b_2 h_2 + p - \frac{1}{2}h_3^2 u_{3x}^2\right)_x = f_3,
\end{aligned} \tag{2}
$$

where

$$
\begin{aligned}
&R = u_1 - \frac{1}{3h_1}\left(h_1^3 u_{1x}\right)_x,\ E = u_3 - \frac{1}{3h_3}\left(h_3^3 u_{3x}\right)_x, \\
&h_2 = H - h_3 - h_1,\ u_2 = \frac{Q(t) - h_3 u_3 - h_1 u_1}{h_2}.
\end{aligned}
$$

When the thickness of the middle layer is reduced to zero $h_2 \to 0$, Equation (1) is transformed into the two-layer model obtained in [8], describing the evolution of internal waves of finite amplitude. Further simplification of the two-layer flow model is obtained after replacing the total derivatives $d_{1,3}/dt$ along the corresponding trajectories of fluid particles by the partial time derivatives $\partial/\partial t$. This simplification corresponds to the transition from a fully nonlinear to a weakly nonlinear model [8].

Now, let us set $h_2 = 0$ in (2) and replace the total derivatives by partial ones. In addition, we consider that under the assumption of smallness of the velocities u_1 and u_3 we have $h_3 u_{3x} + h_1 u_{1x} \simeq -(h_3 + h_1)_t = 0$. As a result, Equation (2) is transformed as follows:

$$
h_{3t} + (h_3 u_3)_x = 0,\ W_t + \left(Wu_1 + U(u_3 - u_1) - \frac{1}{2}u_3^2 + \frac{1}{2}u_1^2 + b_3(h_3 + z)\right)_x = f, \tag{3}
$$

where the following expressions are used:

$$
\begin{aligned}
&h_1 = H - h_3,\ u_1 = \tfrac{Q - h_3 u_3}{h_1},\ f = -\tfrac{c_1 H (u_3 - u_1)|u_3 - u_1|}{h_3 h_1}, \\
&U = \tfrac{1}{H}\left(h_3 W + (H - h_3)u_3 + h_3 u_1 - \tfrac{2}{3} H h_3 h_{3x} u_{3x}\right), \\
&W = u_3 - u_1 - \tfrac{1}{3h_3}\left(h_3^3 u_{3x}\right)_x - \tfrac{1}{3h_1}\left[(H - h_3)^2 h_3\, u_{3x}\right]_x.
\end{aligned}
$$

The constant c_1 is a parameter that determines friction between the fluid layers.

Below, Equations (2) and (3) are used to calculate the evolution of a nonlinear packet of internal waves in the shelf zone and compare the obtained solutions with field observation data. Of course, real stratification in coastal waters is quite complicated. Nevertheless, the approximation of a temperature profile by a two-layer step profile allows us to apply model (3) to calculate the main characteristics of the first-mode internal wave packet, such as amplitude and phase, and to describe their nonlinear interaction.

The results of numerical modeling are compared with field observation data. Modeling (2) and (3) was carried out in such a way that the boundary conditions for these equations were chosen to be the data from thermistor string Sn (n = 1, 2,. . .), and calculations were carried out up to station S(n–m), $m \geq 1$. The quality criterion for mathematical models (2) and (3) was the closeness of the calculation Sn $\to$ S(n–m) and the corresponding field data at thermistor string S(n–m). The good coincidence of the amplitudes and phases of the wave packets allows us to state that we reconstruct, with some acceptable error, the space and time structure of the wave between stations Sn and S(n–m).

4.2. Simulating and Reconstructing

Numerical calculations of the proposed models—Equations (2) and (3)—were carried out on the basis of a computational scheme similar to that proposed for solving the Green–Naghdi model in [43]. The values h_1, h_3, E, R, and W were considered as evolutionary variables, and the velocities u_1 and u_3 were determined at each time step as the solution of the boundary value problem for an ordinary differential equation with given functions h_1, h_{1x}, h_3, h_{3x}, E, R, and W [27].

The values of buoyancy b_2 and b_3 were found from experimental data, and the parameters c_1 and c_2, which determine friction between the water layers and the bottom, were chosen according to the results in [42].

Let us note also that data on the vertical distributions of temperature and velocity along the path between stations are usually not available. Therefore, both spatial distribution of temperature in the layers and horizontal velocity components along the path can be set arbitrarily at the initial moment. However, after some time, sufficient for perturbations to pass from the left boundary through the entire computational domain, the initial data are "forgotten" and the constructed numerical solution can be compared with field data obtained at the control stations.

One of the main goals of our research is to determine the possibility of reconstructing the wave field between buoy stations based on comparison of numerical calculations and field data. For this reason, events that were well identified at several consecutive stations were selected for modeling. Such events usually include long waves and wave bores and, in some cases, they can also be packets of short-period NLIWs. Due to the peculiarities of water stratification, such events are recorded mainly in summer and autumn [26,44]. Therefore, the short-period nonlinear wave packet recorded at station S1 in the interval 321.3–323.5 h of the summer experiment was first selected for modeling. In Figure 7, this time interval is marked with a black rectangle. The leading front of the packet reached S1 at time t_1 = 322.3 h. The wave packet was also recorded at stations S3 and S2. At station S4, this packet is not present; however, a cold-water lens is observed here in the near-bottom region at the moment in the time interval (316 h, 317.8 h). We can assume that its decay is the cause of the formation of this wave packet [33].

Figure 12 shows the results of NLIW package modeling by the three- and two-layer models. Modeling of the package at the point S1 within the three-layer model was carried out using Formula (2), and the temperature values at thermostring S1a were chosen as boundary conditions. The obtained numerical values of the calculation S1a $\rightarrow$ S1 were compared with the experimental data obtained at thermostring S1 at the corresponding time. In the framework of the two-layer model, the calculations S2 $\rightarrow$ S1a and S2 $\rightarrow$ S1 were performed when boundary conditions for model (3) were selected at station S2. The distances between stations were as follows: *Length*(S2, S1a) = 1300 m, *Length*(S1a, S1) = 530 m. The buoyancy values, according to field data, in the lower and intermediate water layers were b_3 = 0.016 m/s^2 and b_2 = 0.008 m/s^2. The friction coefficients were chosen as c_1 = 0.012 and c_2 = 0.004, according to [42]. For the three-layer model, the isothermal surfaces T = 8 °C and T = 14 °C, which were the boundaries of the thermocline, were chosen as surfaces separating the layers. In the two-layer model, two layers of homogeneous fluid were separated by the isothermal surface T = 10 °C. Figure 12 shows that the wave packet recorded at stations S2, S1a, and S1 is significantly nonstationary. The individual waves within the packet interact with each other, so calculation of Sn $\rightarrow$ S(n–m) is rather complicated, and with increasing distance between stations Sn and S(n–m) the difference between the calculated and real isotherms may become more and more apparent. In this case, at the chosen distance (S1a, S1), the three-layer model describes thermocline evolution quite well. As we can see in Figure 12a, the phase and amplitude characteristics of the nonlinear package are close to their calculated values.

Figure 12b presents the wave train calculations by the two-layer model (3), where boundary conditions were taken from station S2, and comparison of the calculated and field data was made at stations S1a and S1. As we can see in Figure 12b, the position of the model isotherm T = 10 °C correctly describes the phase and amplitude characteristics of the real isotherm T = 10 °C even after the wave packet has traveled 1830 m.

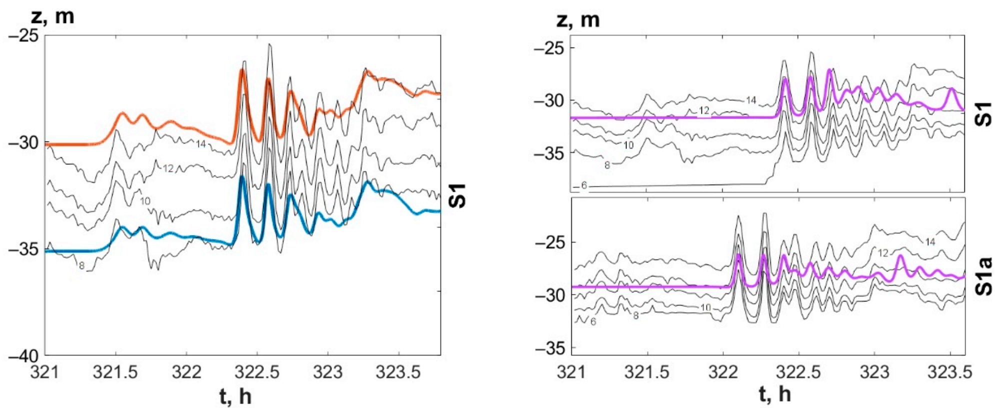

(**a**) (**b**)

Figure 12. Wave packet evolution in the summer of 2022 between stations S2, S1a, and S1. (**a**) Three-layer model calculations (2) S1a → S1, bold lines—calculated isotherms 8 °C (blue) and 14 °C (red), thin lines— isotherms from thermostring S1's data; (**b**) two-layer model calculations (3) S2 → S1a and S2 → S1, bold magenta line—calculated isotherm 10 °C, thin lines—isotherms from thermostrings S1 and S1a's data.

In Figure 13, the results of spatial reconstruction of the flow between stations S1a and S1 at time t = 322.6 h are presented for illustration in accordance with the calculations in Figure 12a. The red line in Figure 13a corresponds to the isotherm 14 °C and the blue line corresponds to the isotherm 8 °C. The black bold line shows the change in the bottom topography $z = z(x)$. The symbol notation corresponds to the parameters in the system of Equation (1). Figure 13b shows the calculated values of flow velocities in all three layers.

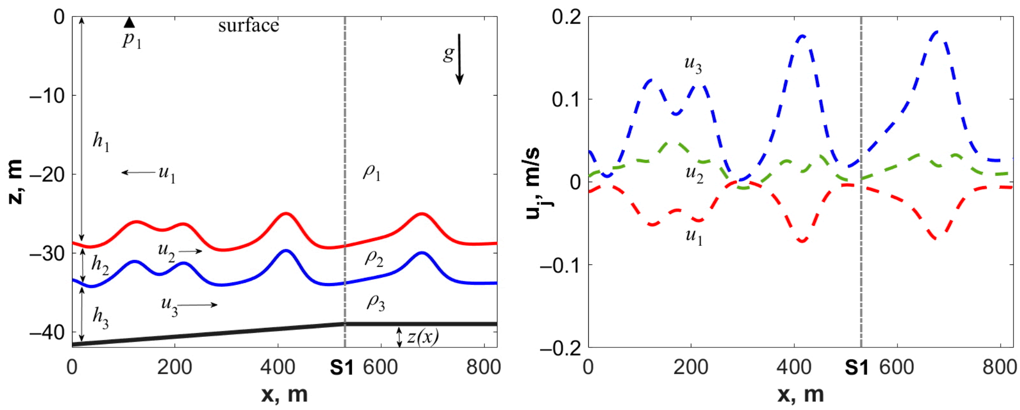

(**a**) (**b**)

Figure 13. (**a**) Spatial reconstruction of the distributions of isotherms 8 °C and 14 °C (solid blue and red lines), the black bold line shows the change in the bottom topography and (**b**) fluid velocities u_1, u_2, and u_3 in the upper, middle, and lower layers (red, green, and blue dashed lines, respectively) calculated by the three-layer model at time t = 322.6 h of the summer experiment. The x = 0 m values correspond to the position of station S1a, the x = 530 m value corresponds to the position of station S1 (marked by vertical line).

Figure 14 shows the results of three-layer modeling of the temperature and flow velocity field in the time interval (173 h, 210 h) (Δt = 37 h) of the autumn experiment from station S3 to stations S2 and S1a. The distances between the stations were as follows: *Length*(S3,S2) = 1970 m, *Length*(S3,S1a) = 3270 m. The Infinity loggers chain was located near station S1a at a distance of 3400 m from S3. The attenuation parameters c_1 and c_2 were chosen to be the same as for the summer experiment. The values of buoyancy, according to field data of the autumn experiment, in the lower and intermediate water layers were equal to $b_3 = 0.02$ m/s^2 and $b_2 = 0.01$ m/s^2.

(a)

(b)

(c)

(d)

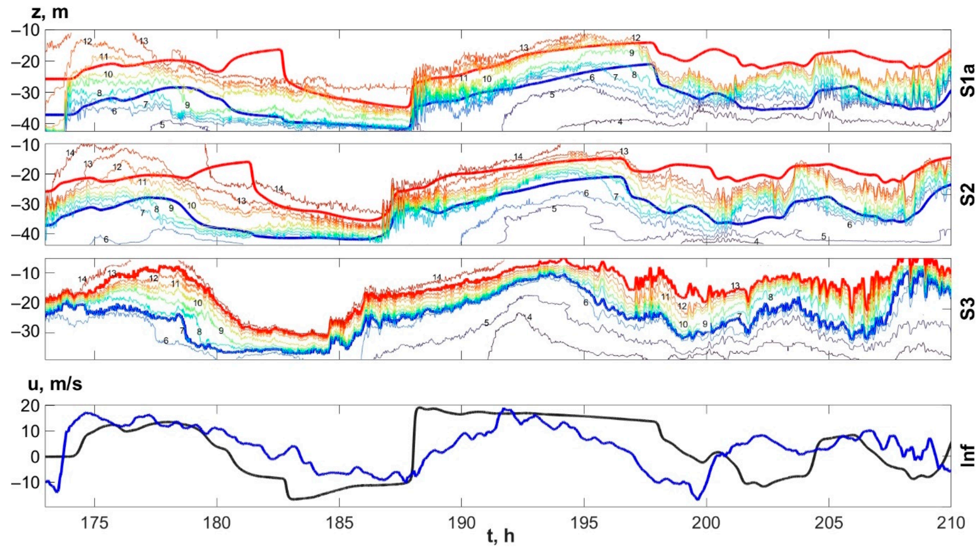

Figure 14. Reconstruction of 37 h of the autumn experiment, with calculations using the three-layer model (2). (**a**) Modeling S3 → S1a and measured temperature at station S1a, isotherms here and hereafter at every 1 °C, bold lines show the calculated isotherms of 7 °C (blue) and 13 °C (red); (**b**) modeling S3 → S2 and measured temperature at station S2, bold lines show the calculated isotherms of 7 °C (blue) and 13 °C (red); (**c**) recorded temperature at station S3; blue and red bold lines are 10 min time-averaged isotherms of 7 °C and 13 °C used as conditions on the left boundary of the computational domain; (**d**) black line is the calculated velocity u_3 in the lower layer, blue line is the value of flow velocity in the direction (S3, S1a) measured by the near-bottom Infinity logger.

In contrast to the simulation results shown in Figure 12, in this case the temperature distribution on thermostring S3 averaged over a time interval of 10 min was used for the boundary conditions of model (2). The isotherms 7 °C and 13 °C were set as the boundaries between homogeneous layers. The choice of an averaging interval of 10 min allowed us to avoid problems of computational scheme stability over a sufficiently long time interval of 37 h.

Figure 14c shows isotherms obtained from field data with a step of 1 °C at station S3. The boundaries of the thermoclines 7 °C and 13 °C are shown in bold lines. In Figure 14a,b, bold lines show the calculated isotherms of 7 °C and 13 °C in the simulations S3 → S2 and S3 → S1a. Thin lines indicate isotherms constructed from field data at stations S2 and S1a, respectively. In Figure 14d, the blue curve corresponds to the 20 min averaged flow velocity values recorded by the Infinity logger installed at 2 m above the bottom. The black curve describes the values of velocity u_3 obtained in the process of modeling Equation (2) with boundary condition corresponding to the averaged field data from station S3. Let us note also that in the selected time interval (173 h, 210 h), the formation of several bores is observed, e.g., at times t = 174 h and t = 188 h at the shallow-water station.

As we can see in Figure 14, at the specified distances, model (2) with the selected averaged boundary values does not describe the high-frequency component of the temperature field (periods less than 10–20 min). However, it quite satisfactorily describes long-wave processes, i.e., it approximates the phase and amplitude of the real long wave of the first and second modes. The compression–stretching and ascent–descent of the isotherms corresponds to the behavior of isotherms (isopycnic lines) obtained from field data. The qualitatively correct calculated value of velocity u_3 describes the real near-bottom flow and, in general, correctly determines its phase and amplitude.

5. Discussion and Conclusions

In the paper, we have presented the results of NLIW measurements at the hydrophysical test site in the southwestern part of the Sea of Japan. The experimental data obtained by the authors of this paper and the presented results are unique. The authors of the paper have been carrying out experiments at this site for twelve years and in different seasons of the year. The main measuring instruments for recording NLIWs were moored thermostrings. Thermostrings were arranged in two clusters in such a way as to classify various structures of internal waves, determine the direction of their movement, evaluate various kinematic characteristics, etc. For example, we have established that in this area the phase velocity of the NLIWs varies in the range of 0.2–0.6 m/s; the predominant direction of movement of the NLIW packets is 336°, which corresponds to the direction of the barotropic tide movement. The arrangement of thermostrings along this direction allowed us to record the space and time structure of the internal wave bore during its movement toward the shore (Figure 11). We found that the greatest number of events of internal waves is observed in autumn, when the thermocline is located near the bottom, and the thermal structure of the waters is either two- or three-layered. We have shown that after the bore passage, the initial stratification of water can either be preserved or completely destroyed in a fairly short time. The latter fact is especially important for applied problems of underwater sound formation in the shelf zone. Such a radical change in the structure of the temperature field, and hence, the speed of sound, will inevitably lead to a significant rearrangement of the sound field mode structure.

Mathematical models describing the evolution of NLIWs can be divided into three groups [6,45]. The first group, nonlinear models, includes equations derived using asymptotic methods in the approximation of low nonlinearity and low dispersion. Among these approximate models, the most popular model is the KdV equation for internal waves. Models of the second group include various generalizations of the KdV equation of higher orders in nonlinearity and dispersion; see, for example, [46,47]. This group also includes models developed on the basis of the Green–Naghdi-type equation systems. These models include full nonlinearity and dispersion and have been developed for both two-layer [8] and multi-layer oceans [28,48]. In recent years, models based on nonlinear Euler or Navier–Stokes equations, taking into account the bottom topography and rotation of the Earth, have been actively developed [49,50]. We relate these models to the third group.

As we demonstrated in Section 3, the site we chose is characterized by highly nonlinear internal wave processes. For this reason, the models of the first group were not sufficient for us. Models of the third group require large computational resources and additional oceanological information beyond the measurements obtained only by thermostring clusters. In addition, the purpose of this study was to construct relatively simple models of thermocline deformation in the shelf zone of the sea, allowing, based on field data obtained at the experimental site, the reconstruction of short-period and long-wave processes associated with the passage of intense internal waves. For this reason, we chose models of the second group. Preference was given to completely nonlinear equations of the Green–Naghdi type, namely, multi-layer shallow water equations in the second-order approximation. To simplify the calculations, we limited ourselves to two- and three-layer models. Additional simplification of the three-layer model was in choosing the hydrostatic condition for the intermediate layer, which, as we noted in Section 4, does not affect the structure of large-amplitude near-bottom waves.

We can propose the following arguments in favor of our choice and subsequent use of models (2) and (3).

As we know, within the framework of weakly nonlinear and moderately nonlinear models, which are reduced to modifications of the KdV equation (for example, the Gardner equation), in which the coefficients are determined by the initial unperturbed stratification, transformation of a depression wave upon reaching the shore leads to a change in the "polarity" of the wave, i.e., its transformation into an elevation wave [51,52]. Substantially nonlinear models, including (2) and (3), demonstrate a more complex process of flattening the leading front and steepening of the trailing front of a sufficiently long internal depression wave, leading to formation of an internal wave bore [27,35].

We should note that not all phenomena observed in our experiments can be simulated based on the modified KdV equations. For example, it is problematic to describe the structure and dynamics of near-bottom isolated lenses of colder water during the "splash" of NLIWs into the coastal zone. However, this can be achieved within the framework of models (2) and (3) [33].

It is worth emphasizing separately that the validity of the choice of two- and three-layer models was checked in the process of the experiments and of their comparison with calculations. Such comparisons were made by the authors in a whole series of works, for example, [8,27,28,33]. In [28], in addition to models (2) and (3), a multi-layer model was considered. As an example, the authors carried out calculations for a model of six layers. As a result of such studies, it was shown that simplified models of two- and three-layer shallow water, taking into account the non-hydrostatic pressure distribution in one or several layers, are applicable for describing the evolution of nonlinear wave packets in coastal waters with rather complex density stratification and vertical velocity shifts.

As we have already noted in the Introduction, one of the pressing problems of modern oceanology is the reconstruction of hydrophysical fields measured at individual points in the ocean. In our case, in a two-dimensional description, the problem is stated as follows: using data from temperature profile fluctuations at a deeper-water station, restore the amplitude–frequency characteristics of a wave packet propagating toward the shore and, in particular, compare them with the recording of similar characteristics at a shallower-water station. In [6], this approach is implemented using a single evolutionary equation. At the same time, due to the too large distance between neighboring stations, it was not possible to achieve a good coincidence in phases and amplitudes of the calculated and measured waves at the control station.

In this paper, we used models (2) and (3) to reconstruct the temperature distribution. Let us note that data on the vertical distribution of temperature and velocity along the path between stations, as a rule, are missing. Therefore, both spatial distribution of temperature in the layers and horizontal velocity components along the path at the initial moment can be specified arbitrarily. However, after some time, sufficient for passage of disturbances from the left boundary through the entire computational domain, the initial data are "forgotten" and the constructed numerical solution can be compared with field data obtained at control stations.

The results of such a reconstruction were presented in Figures 12–14.

We established that for waves with periods of more than 10 min, calculations are in good agreement with experiment at distances of the order of 1 km—Figure 12. At distances up to 4 km (possibly even more), low-frequency processes are described quite satisfactorily—Figure 14.

It is shown that models (2) and (3), based only on data on vertical temperature distribution obtained from the deep-water thermostring, allow us to correctly restore the phase and amplitude of bottom flows at the points where the shallow-water thermostring was moored—Figure 14d.

The obtained results allow us to hope for a successful solution of the above problem of temperature reconstruction by way of the correct arrangement of thermostrings in a specific water area. The use of various temperature and salinity regression methods [26] will thus allow the reconstruction of various hydrophysical fields in a specific sea area.

In conclusion, we would like to note the following.

This paper, in our view, makes a significant contribution to the existing research on internal waves conducted by other authors in this region. As mentioned in the Introduction, the majority of similar studies were based on field observations, episodic both in year and in season. However, NLIW generation and propagation conditions can vary from year to year. Long-term observations using thermostring clusters have allowed us to understand the general pattern of NLIW propagation and transformation on the shelf of Peter the Great Bay. For this reason, we selected 2022 for this study, as it represented typical wave propagation conditions observed over the previous 12 years. This allowed us to determine or clarify important parameters of internal waves, such as phase velocities, the movement direction of wave packets, classify different types of bores, estimate seasonal event statistics, and more. In particular, the spatial distribution of the thermostrings allowed us to record spatial transformation of an undular bore as it moved toward the shore.

Some experimental results and proposed approaches may be interesting and useful for internal wave researchers working in a wide variety of shelf zones of the world's oceans.

- First of all, this is a methodology for systematic long-term observations based on thermostring clusters, which allows us to systematize the obtained data in space and time. According to the literature we are aware of, such experiments are still rare.
- The determined effects of increased vertical mixing of water during the movement of an internal nonlinear structure, e.g., a bore. This problem is interesting and needs theoretical explanation.
- Two- and three-layer fully nonlinear internal wave models tested on real strongly nonlinear and nonstationary processes.
- The methodology for reconstructing nonlinear wave fields between thermostrings. The development of this methodology is relevant not only for applied tasks but also for theoretical research, such as in hydroacoustics, navigation, and underwater communication.

Author Contributions: Conceptualization, I.Y. and V.L.; methodology, I.Y. and V.L.; software, V.L. and A.K.; validation, O.G., R.K., A.S. (Alex Shvyrev) and F.K.; formal analysis, I.Y.; investigation and experimental studies, I.Y., A.P., A.S. (Aleksandr Samchenko), A.S. (Alex Shvyrev) and F.K.; resources, A.P.; data curation, A.K.; writing—original draft preparation, I.Y. and V.L.; writing—review and editing, I.Y., V.L. and A.K.; visualization, V.L., A.K. and A.S. (Alex Shvyrev); supervision, I.Y. and G.D.; project administration, I.Y. and G.D.; funding acquisition, G.D. All authors have read and agreed to the published version of the manuscript.

Funding: The authors appreciate the support of theoretical studies by the Laboratory of Nonlinear Hydrophysics and Natural Hazards of POI FEB RAS, a project of the Ministry of Science and Education of Russia, project No. 075–15-2022–1127. The experimental studies were carried out as a part of the Russian State assignment, registration numbers: 124022100074–9 and FWGG–2021–0011–2.3.1.2.12.

Institutional Review Board Statement: Not applicable.

Informed Consent Statement: Not applicable.

Data Availability Statement: Experimental data are archived at the Laboratory of Statistical Hydroacoustics (POI FEB RAS) and available upon request with some restrictions apply to the availability of these data.

Conflicts of Interest: The authors declare no conflicts of interest.

References

1. Holloway, P.E. Internal hydraulic jumps and solitons at a shelf break region on the Australian North West Shelf. *J. Geophys. Res.* **1987**, *92*, 5405–5416.
2. Helfrich, K.R.; Melville, W.K. Long Nonlinear Internal Waves. *Annu. Rev. Fluid Mech.* **2006**, *38*, 395–425. [CrossRef]
3. Walter, R.K.; Woodson, C.B.; Arthur, R.S.; Fringer, O.B.; Monismith, S.G. Nearshore internal bores and turbulent mixing in southern Monterey Bay. *J. Geophys. Res.* **2012**, *117*, C07017. [CrossRef]
4. Serebryany, A.; Khimchenko, E.; Popov, O.; Denisov, D.; Kenigsberger, G. InternalWaves Study on a Narrow Steep Shelf of the Black Sea Using the Spatial Antenna of Line Temperature Sensors. *J. Mar. Sci. Eng.* **2020**, *8*, 833. [CrossRef]
5. Talipova, T.G.; Pelinovsky, E.N.; Lamb, K.; Grimshow, R.; Holloway, P. Cubic nonlinearity effects in the propagation of intense internal waves. *Dokl. Earth Sci.* **1999**, *364*, 824–827.
6. Talipova, T.G.; Pelinovsky, E.N.; Kurkin, A.A.; Kurkina, O.E. Modeling the dynamics of intense internal waves on the shelf. *Izv. Atmos. Ocean. Phys.* **2014**, *50*, 630–637. [CrossRef]
7. Craig, W.; Guyenne, P.; Kalisch, H. Hamiltonian long-wave expansions for free surfaces and interfaces. *Commun. Pure Appl. Math.* **2005**, *58*, 1587–1641. [CrossRef]
8. Choi, W.; Camassa, R. Fully nonlinear internal waves in a two-fluid system. *J. Fluid Mech.* **1999**, *386*, 1–36. [CrossRef]
9. Liapidevskii, V.Y.; Novotryasov, V.V.; Khrapchenkov, F.F.; Yaroshchuk, I.O. Internal Wave Bore in the Shelf Zone of the Sea. *J. Appl Mech. Tech. Phys.* **2017**, *58*, 809–818. [CrossRef]
10. Cherkesov, L.V.; Potetunko, E.N.; Shubin, D.S. Reconstruction of ocean density distribution from its wave spectrum. *Int. J. Fluid Mech. Res.* **2003**, *30*, 11–23. [CrossRef]

11. Makarenko, N.I.; Perevalova, E.G. Density stratification and amplitude dispersion of internal waves. *Fundam. Prikl. Gidrofiz.* **2013**, *2*, 71–77. (In Russian)
12. Ocherednik, V.V.; Zatsepin, A.G.; Kuklev, S.B.; Baranov, V.I.; Mashura, V.V. Examples of Approaches to Studying the Temperature Variability of Black Sea Shelf Waters with a Cluster of Temperature Sensor Chains. *Oceanology* **2020**, *60*, 149–160. [CrossRef]
13. Serebryany, A.N. Internal waves in a coastal zone of a tidal sea. *Oceanology* **1985**, *25*, 744–751. (In Russian)
14. Serebryany, A.N. Internal waves on a shelf and in vicinity of continental slope as registered by towed line temperature sensor. *Oceanology* **1987**, *27*, 225–226. (In Russian)
15. Navrotsky, V.V.; Ilyichev, V.I. Vertical structure of hydrophysical characteristics and internal waves near the shelf boundary. *GeoJournal* **1988**, *16*, 11–17. [CrossRef]
16. Novotryasov, V.V.; Karnaukhov, A.A. Nonlinear Interaction of Internal Waves in the Coastal Zone of the Sea of Japan. *Izv. Atmos. Ocean. Phys.* **2009**, *45*, 262–270. [CrossRef]
17. Rybak, S.A.; Serebryanyi, A.N. Nonlinear internal waves over the inclined bottom: Observations with the use of an acoustic profiler. *Acoust. Phys.* **2011**, *57*, 77–82. [CrossRef]
18. Sabinin, K.D.; Serebryanyĭ, A.N. "Hot spots" in the field of internal waves in the ocean. *Acoust. Phys.* **2007**, *53*, 357–380. [CrossRef]
19. Navrotsky, V.V.; Izergin, V.L.; Pavlova, E.P. Generation of internal waves near the shelf boundary. *Dokl. Earth Sci.* **2003**, *388*, 84–88. Available online: https://www.researchgate.net/publication/297414462 (accessed on 1 April 2024).
20. Novotryasov, V.V.; Zakharkov, S.P.; Stepanov, D.V. Internal tides in the coastal zone of the Sea of Japan in autumn. *Russ. Meteorol. Hydrol.* **2016**, *41*, 564–568. [CrossRef]
21. Konstantinov, O.G.; Novotryasov, V.V. Surface manifestations of internal waves observed using a land-based video system. *Izv. Atmosph. Oceanic. Phys.* **2013**, *49*, 334–338. [CrossRef]
22. Navrotsky, V.V.; Lozovatsky, I.D.; Pavlova, E.P.; Fernando, H.J.S. Observations of the internal waves and thermocline splitting near a shelf break of the Sea of Japan (East Sea). *J. Cont. Shelf Res.* **2004**, *24*, 1375–1395. [CrossRef]
23. Novotryasov, V.V.; Stepanov, D.V.; Yaroshchuk, I.O. Observation of internal bores on the Japan/East Sea shelf-coastal region. *Ocean Dyn.* **2016**, *66*, 19–25. [CrossRef]
24. Kokoulina, M.V.; Kurkina, O.E.; Talipova, T.G.; Kurkin, A.A.; Pelinovsky, E.N. Average Climatic Characteristics of Internal Waves in the Sea of Japan Based on the WOA18 Atlas. *Phys. Oceanogr.* **2023**, *30*, 563–580.
25. Leontyev, A.P.; Yaroshchuk, I.O.; Smirnov, S.S.; Kosheleva, A.V.; Pivovarov, A.A.; Samchenko, A.N.; Shvyrev, A.N. A spatially distributed measuring complex for monitoring hydrophysical processes on the ocean shelf. *Instrum. Exp. Technol.* **2017**, *60*, 130–136. [CrossRef]
26. Yaroshchuk, I.O.; Kosheleva, A.V.; Lazaryuk, A.Y.; Dolgikh, G.I.; Pivovarov, A.A.; Samchenko, A.N.; Gulin, O.E.; Korotchenko, R.A. Estimation of Seawater Hydrophysical Characteristics from Thermistor Strings and CTD Data in the Sea of Japan Shelf Zone. *J. Mar. Sci. Eng.* **2023**, *11*, 1973. [CrossRef]
27. Kukarin, V.F.; Liapidevskii, V.Y.; Khrapchenkov, F.F.; Yaroshchuk, I.O. Nonlinear internal waves in the shelf zone of the sea. *J. Fluid Dyn.* **2019**, *54*, 329–338. [CrossRef]
28. Liapidevskii, V.Y.; Khrapchenkov, F.F.; Chesnokov, A.A.; Yaroshchuk, I.O. Modeling of unsteady geophysical processes on the shelf of the Sea of Japan. *Fluid Dyn.* **2022**, *57*, 55–65. [CrossRef]
29. Thomson, R.E.; Emery, W.J. *Data Analysis Methods in Physical Oceanography*, 3rd ed.; Elsevier: Amsterdam, The Netherlands, 2014; 716p. [CrossRef]
30. Kokoulina, M.V.; Kurkina, O.E.; Rouvinskaya, E.A.; Kurkin, A.A. Probabilistic characteristics of intensive short-period internal waves in the Sea of Japan. *Phys. Oceanogr.* **2020**, *27*, 501–513. [CrossRef]
31. Lynch, J.F.; Jin, G.; Pawlowicz, R.; Ray, D.; Chiu, C.-S.; Miller, J.H.; Bourke, R.H.; Parsons, A.R.; Muecnh, R. Acoustic travel-time perturbations due to shallow-water internal waves and internal tides in the Barents Sea Polar Front: Theory and experiment. *J. Acoust. Soc. Am.* **1996**, *99*, 803–821. [CrossRef]
32. Yang, T.C.; Yoo, K. Internal Wave Spectrum in Shallow Water: Measurement and Comparison with the Garrett–Munk Model. *IEEE J. Ocean. Eng.* **1999**, *24*, 333–345. [CrossRef]
33. Kosheleva, A.V.; Liapidevskii, V.Y.; Khrapchenkov, F.F.; Yaroshchuk, I.O. Spatial evolution of near-bottom cold-water lenses of the shelf of Sea of Japan. *J. Appl. Mech. Tech. Phys.* **2023**, *64*, 455–464. [CrossRef]
34. Holloway, P.E.; Pelinovsky, E.; Talipova, T.; Barnes, B. A Nonlinear Model of Internal Tide Transformation on the Australian North West Shelf. *J. Phys. Oceanogr.* **1997**, *27*, 871–896. [CrossRef]
35. Bourgault, D.; Blokhina, M.D.; Mirshak, R.; Kelley, D.E. Evolution of a shoaling internal solitary wavetrain. *J. Geophys. Res.* **2007**, *34*, L03601. [CrossRef]
36. Colosi, J.A.; Kumar, N.; Suanda, S.H.; Freismuth, T.M.; MacMahan, J.H. Statistics of internal tide bores and internal solitary waves observed on the continental shelf of Point Sal, California. *J. Phys. Oceanogr.* **2018**, *48*, 123–143. [CrossRef]
37. Henyey, F.S.; Hoering, A. Energetics of borelike internal waves. *J. Geophys. Res.* **1997**, *102*, 3323–3330. [CrossRef]
38. Apel, J.R.; Stepanyants, Y.A.; Lynch, J.F. Internal solitons in the ocean and their effect on underwater sound. *J. Acoust. Soc. Am.* **2007**, *121*, 695–722. [CrossRef]
39. Brekhovskikh, L.M.; Konyaev, K.V.; Sabinin, K.D.; Serikov, A.N. Short-period internal waves in the sea. *J. Geophys. Res.* **1975**, *80*, 856–864. [CrossRef]

40. Liapidevskii, V.Y.; Teshukov, V.M. *Mathematical Models of Propagation of Long Waves in Inhomogeneous Fluid*; Publishing House of the Siberian Branch of the Russian Academy of Sciences: Novosibirsk, Russia, 2000. (In Russian)
41. Helfrich, K.R. Decay and return of internal solitary waves with rotation. *Phys. Fluids.* **2007**, *19*, 026601. [CrossRef]
42. Gavrilov, N.; Liapidevskii, V.; Gavrilova, K. Large amplitude internal solitary waves over a shelf. *Natur. Hazards Earth Syst. Sci.* **2011**, *11*, 17–25. [CrossRef]
43. Le Metayer, O.; Gavrilyuk, S.; Hank, S. A Numerical Scheme for the Green–Naghdi Model. *J. Comput. Phys.* **2010**, *229*, 2034–2045. [CrossRef]
44. Novotryasov, V.V.; Pavlova, E.P.; Permyakov, M.S. Internal tidal fronts in the coastal zone of the Japan Sea. *Russ. Meteorol. Hydrol.* **2015**, *40*, 109–114. [CrossRef]
45. Lamb, K.G.; Yan, L. The evolution of internal wave undular bores: Comparisons of a fully nonlinear numerical model with weakly nonlinear theories. *J. Phys. Oceanogr.* **1996**, *26*, 2712–2734. [CrossRef]
46. Kamchatnov, A.M.; Kuo, Y.-H.; Lin, T.-C.; Horng, T.-L.; Gou, S.-C.; Clift, R.; El, G.A.; Grimshaw, R.H.J. Undular bore theory for the Gardner equation. *Phys. Rev. E* **2012**, *86*, 036605. [CrossRef] [PubMed]
47. Kurkina, O.; Pelinovsky, E. Nonlinear Transformation of Sine Wave within the Framework of Symmetric (2+4) KdV Equation. *Symmetry* **2022**, *14*, 668. [CrossRef]
48. Choi, W. Modeling of Strongly Nonlinear Internal Gravity Waves. In Proceedings of the 4th International Conference on Hydrodynamics, Yokohama, Japan, 7–9 September 2000.
49. Vlasenko, V.; Stashchuk, N. Three-dimensional shoaling of large-amplitude internal waves. *J. Geoph. Res.* **2007**, *112*, C11018. [CrossRef]
50. Zhang, Z.; Fringer, O.D.; Ramp, S.R. Three-dimensional, nonhydrostatic numerical simulation of nonlinear internal wave generation and propagation in the South China Sea. *J. Geoph. Res.* **2011**, *116*, C05022. [CrossRef]
51. Grimshaw, R.; Pelinovsky, E.; Talipova, T. Solitary wave transformation in a medium with sign-variable quadratic nonlinearity and cubic nonlinearity. *Phys. D* **1999**, *132*, 40–62. [CrossRef]
52. Serebryany, A.; Pao, H. Transition of a nonlinear internal wave through an overturning point on a shelf. *Dokl. Earth Sci.* **2008**, *420*, 714–718. [CrossRef]